

# The nature of plasmon excitations in hole-doped cuprate superconductors

Abhishek Nag,<sup>1,\*</sup> M. Zhu,<sup>2</sup> Matías Bejas,<sup>3</sup> J. Li,<sup>1,4</sup> H. C. Robarts,<sup>1,2</sup> Hiroyuki Yamase,<sup>5,6</sup> A. N. Petsch,<sup>2</sup> D. Song,<sup>7</sup> H. Eisaki,<sup>7</sup> A. C. Walters,<sup>1</sup> M. García-Fernández,<sup>1</sup> Andrés Greco,<sup>3</sup> S. M. Hayden,<sup>2,†</sup> and Ke-Jin Zhou<sup>1,‡</sup>

<sup>1</sup>*Diamond Light Source, Harwell Campus, Didcot OX11 0DE, United Kingdom*

<sup>2</sup>*H. H. Wills Physics Laboratory, University of Bristol, Bristol BS8 1TL, United Kingdom*

<sup>3</sup>*Facultad de Ciencias Exactas, Ingeniería y Agrimensura and Instituto de Física Rosario (UNR-CONICET), Av. Pellegrini 250, 2000, Rosario, Argentina*

<sup>4</sup>*Beijing National Laboratory for Condensed Matter Physics, Institute of Physics, Chinese Academy of Sciences, Beijing 100190, China*

<sup>5</sup>*National Institute for Materials Science, Tsukuba 305-0047*

<sup>6</sup>*Department of Condensed Matter Physics, Graduate School of Science, Hokkaido University, Sapporo 060-0810, Japan*

<sup>7</sup>*National Institute of Advanced Industrial Science and Technology (AIST), Tsukuba, Ibaraki 305-8560, Japan*

High  $T_c$  superconductors show a rich variety of phases associated with their charge degrees of freedom. Valence charges can give rise to charge ordering or acoustic plasmons in these layered cuprate superconductors. While charge ordering has been observed for both hole- and electron-doped cuprates, acoustic plasmons have only been found in electron-doped materials. Here, we use resonant inelastic X-ray scattering (RIXS) to observe the presence of acoustic plasmons in two families of hole-doped cuprate superconductors [ $\text{La}_{2-x}\text{Sr}_x\text{CuO}_4$  (LSCO) and  $\text{Bi}_2\text{Sr}_{1.6}\text{La}_{0.4}\text{CuO}_{6+\delta}$  (Bi2201)], crucially completing the picture. Interestingly, in contrast to the quasi-static charge ordering which manifests at both Cu and O sites, the observed acoustic plasmons are predominantly associated with the O sites, revealing a unique dichotomy in the behaviour of valence charges in hole-doped cuprates.

High temperature superconductivity emerges in cuprates when electrons or holes are introduced to the  $\text{CuO}_2$  planes of the parent antiferromagnetic insulators [1]. Their electronic structure may be understood in terms of a hybridisation between the Cu  $3d_{x^2-y^2}$  and O  $2p_\sigma$  orbitals, and a strong on-site Coulomb repulsion between electrons on the Cu sites [2–5]. When holes are introduced (see Fig. 1(a, b)), they reside preferentially in the so-called “charge-transfer band” (CTB) which is composed primarily of O orbitals [6]. In contrast, doped electrons enter the upper Hubbard band (UHB) and primarily reside on the Cu sites [5]. Despite this asymmetry in the electronic structure, charge order, a complex phase of periodically modulated charge-carrier density, has been observed ubiquitously on both the electron- and hole-doped sides of the phase diagram [7].

Surprisingly, a more widely observed mode of collective charge density oscillation, the acoustic plasmon [8], has been rather elusive for the cuprates. In contrast to three-dimensional (3D) metals, where long-range Coulomb interactions give rise to isotropic long-wavelength optical-like gapped plasmons, out-of-phase oscillations of charges in neighbouring planes of two-dimensional (2D) layered electron gases, form acoustic plasmons, whose energy tends to zero for small in-plane wavevectors (see Fig. 1(c)) [9, 10]. Due to the confinement of the doped-charges to the  $\text{CuO}_2$  planes and the poor screening of out-of-plane Coulomb interactions by the intervening dielectric blocks (see Fig. 1(d)), acoustic plasmons are also expected in the layered cuprates [5, 11, 13].

A remarkable discovery has been the recent observation

of acoustic plasmons in electron-doped  $\text{La}_{2-x}\text{Ce}_x\text{CuO}_4$  (LCCO) and  $\text{Nd}_{2-x}\text{Ce}_x\text{CuO}_4$  (NCCO) [14, 15] using Cu  $L_3$ -RIXS, owing to improvements in energy-resolution and the ability to probe in- and out-of-plane momenta independently. The excitations detected in the electron-doped superconductors showed the strong out-of-plane dispersion expected for plasmons in layered systems. The situation in hole-doped cuprates, however, has remained rather controversial. While Cu  $L_3$ -RIXS did not detect plasmons in several hole-doped families [16–18], O  $K$ -RIXS did detect excitations in  $\text{La}_{2-x}(\text{Br},\text{Sr})_x\text{CuO}_4$  that were interpreted as incoherent intra-band transitions [19]. Also recently, electron energy-loss spectroscopy, a traditional probe for studying plasmons, found only featureless non-dispersive charge excitations in hole-doped  $\text{Bi}_{2.1}\text{Sr}_{1.9}\text{CaCu}_2\text{O}_{8+\delta}$  [20]. There is much evidence for the existence of the low-energy quasiparticle states in cuprates, for example, from angle-resolved photoemission studies [21]. Since plasmons originate from the existence of conduction electrons, long-range nature of the Coulomb interaction, their absence in hole-doped cuprates conflicts with our general understanding of the collective behaviour of the doped-charges. Here we report that acoustic plasmons are indeed present in hole-doped cuprates. We make an extensive O  $K$ -RIXS study of the LSCO and Bi2201 systems over a wide range of in- and out-of-plane momenta.

Spectroscopically, Cu  $L_3$ - and O  $K$ -RIXS directly probe the charge and magnetic excitations associated with the Cu  $3d$  and O  $2p$  orbitals, respectively, at the corresponding absorption peaks (Fig. 1(a)). In order to compare the excitations associated with the two orbitals, a survey was made at both edges near the in-plane zone-centre with a fixed scattering angle on Bi2201 (Fig. 1(e, f)). The low-energy inelastic spectra at Cu  $L_3$  resonance are dominated by paramagnon excitations without any noticeable

\* Email: abhishek.nag@diamond.ac.uk

† Email: s.hayden@bristol.ac.uk

‡ Email: kejin.zhou@diamond.ac.uk

signs of plasmon-like excitations, similar to previous reports on other hole-doped systems [16–18]. At the O  $K$ -edge *hole*-peak however [6], a mode is found below 1 eV, dispersing towards the zero-energy in both materials (see also Extended Data Fig. 1).

We next collected RIXS spectra by varying the incident energy ( $E_i$ ) across the hole-peak in O  $K$ -edge X-ray absorption (XAS) of LSCO (Fig. 1(b)) [6], as shown in Fig. 1(g). We find a broad feature at  $\sim 0.5$  eV shifting towards higher energies with increasing  $E_i$ . With doping, the probability of scattering from doped-charges in the intermediate state of RIXS increases [22]. Moreover, energy-shift of the magnetic excitations associated with incoherent charge excitations is enhanced in  $\sigma$ -polarised RIXS (see Methods A) [23]. Thus this feature, can be ascribed to bimagnon excitations, with an itinerant character [22]. Owing to the improved energy-resolution and low  $h$ -value (0.03), we find an additional sharp mode, at  $\sim 0.13$  eV, whose energy remains constant with  $E_i$ . This is a signature of its coherent nature [15] and is in contrast with previous O  $K$ -RIXS results [19]. This feature cannot be due to two-particle electron-hole like excitations, which are incoherent in nature. Neither can it be due to single-magnons or paramagnons since  $\Delta S = 1$  spin-flip processes are forbidden at the O  $K$ -edge [22]. To ascertain its origin, we explored further its dispersion in energy-momentum space.

The broad feature seen in Fig. 1(g) is almost non-dispersive in the  $h$ -direction further confirming its assignment as bimagnons [22]. This can be seen from  $(h, E)$ -maps collected at constant  $l$ -values for LSCO and Bi2201 (Fig. 2(a-d)). In contrast, the sharp mode disperses towards zero energy near the in-plane zone-centre in both systems. The dispersion and reduction of amplitude and width towards the in-plane zone-centre of this mode, is reminiscent of the acoustic plasmon behaviour observed in electron-doped LCCO [14]. However, the mode is strongly damped in comparison (Extended Fig. 3(d)), reflecting the stronger correlations (e.g. pseudogap) near optimal doping in hole-doped cuprates [5, 15].

The most stringent test for identifying the modes as plasmons in these systems is their  $l$ -dispersion. In the out-of-plane direction, plasmons in layered electron systems have a periodicity of  $\pi/d$  (where  $d$  is the interlayer spacing between the layers), which corresponds to  $l = 2$  in these systems, with a minimum in energy at  $l = 1, 3, 5 \dots$  (Fig. 1(c)). LSCO and Bi2201 have interlayer spacings which differ by a factor of  $\sim 2$ , allowing us to probe a significant portion of this period. The sharp mode observed in Fig. 2, is found to disperse to a minimum energy value at  $l = 1$  for both the systems. This can be seen in the  $(l, E)$ -maps collected at fixed  $h$ -values shown in Fig. 3(a-d). This behaviour fundamentally proves the presence of acoustic plasmons in hole-doped cuprates. We can exclude the previous interpretation of these excitations as incoherent intra-band charge or electron-hole excitations which are 2D [19], without significant  $l$ -dependence [5]. Our LSCO results are consistent with a limited out-of-plane dispersion study done recently [24].

The cuprates are strongly correlated electron sys-

tems [1]. As such, it is interesting to compare our experimental results with the recently developed calculations of plasmons in the framework of a  $t$ - $J$ - $V$  model (see Methods C and Supplementary Information IV) [5], although generic plasmon behaviour can also be described within random-phase-approximation calculations [11, 13]. The model is given 3D character by incorporating long-range bare Coulomb interaction  $V(\mathbf{Q})$  and interlayer hopping  $t_z$ . The imaginary part of charge susceptibility  $\chi''(\mathbf{Q}, \omega)$ , obtained from the model resembles well the spectral shape of the plasmons for both systems, as shown in Fig. 3(f) at different  $(h, l)$ -values. This demonstrates that the charge excitations in RIXS, although influenced by resonance and polarisation effects, can fundamentally be related to the charge-density response function. At  $l$ -values close to 2, the much larger suppression of plasmons compared to theory could be due to their decay through the incoherent charge channels associated with bimagnons or through Umklapp scattering [14]. Severe suppression of the charge excitations in this region forbids us from even detecting the optical plasmon branch in Bi2201 (see Extended Data Fig. 2). In Fig. 4(a-c) we show that both the  $h$ - and  $l$ -direction plasmon dispersions extracted by fitting the RIXS spectra for LSCO and Bi2201 are also represented well by the  $t$ - $J$ - $V$  model. The higher acoustic plasmon velocities in Bi2201 than LSCO seen in Fig. 4(a, b), arise mainly due to the larger interlayer spacing, considering the two systems have similar carrier densities and Fermi velocities (see Supplementary Information Fig. S11) [9, 14]. Nevertheless, the remarkable similarity of the plasmon dispersions in the two different families suggests their ubiquitous existence in hole-doped cuprates.

In order to shed light on the possible existence of plasmons at Cu sites, we use the model described above to calculate the expected plasmon energies (see solid lines) for both systems along the  $(h, l)$ -paths corresponding to the data shown in Fig. 1(e, f) and Extended Fig. 1. For Bi2201, the experiment probes near  $l = 3$ , where the plasmons are expected to be strong. There is no evidence for plasmon excitations (Fig. 1(e)). Likewise, for LSCO, no plasmon spectral weight is observed near  $l = 1.8$  (Extended Fig. 1(a)). However, plasmons were observed in electron-doped LCCO using Cu  $L_3$ -RIXS at similar  $l$ -values as in LSCO [14]. Our high-resolution data close to the in-plane zone-centre and wide range of  $l$ -values therefore indicate the absence of plasmons at the Cu sites in hole-doped cuprates [16, 17]. This contrasts with the strong signals observed at the O sites.

It is interesting to discuss our findings in the context of the charge order type of density modulation observed in hole-doped cuprates using both Cu  $L_3$ - and O  $K$ -edge resonant X-ray scattering [25–27]. In common with other charge-density waves, the order has a valence charge modulation and associated atomic displacements [28], making it possible to be observed by non-resonant X-ray scattering techniques [29]. As such, it is likely that, in these systems, the charge ordering signal observed at the Cu  $L_3$  absorption peak is primarily owing to atomic displacements caused by electron-phonon coupling, while

the dominant signal at the O  $K$  hole-peak reflects directly the valence charge modulation [26, 30]. Due to the much higher frequencies of the dynamic plasmons, it may be that they couple weakly to the phonons, thereby reducing the possibility to observe any signature directly from the Cu  $3d$  orbitals.

The discovery of acoustic plasmons in the hole-doped systems remarkably illustrates the universal existence of low-energy collective excitations besides phonons and spin-fluctuations across the cuprate phase diagram. The general existence of acoustic plasmons may stimulate more studies of charge dynamics in connection with the pseudogap phase, non-Fermi liquid behaviour and perhaps the superconductivity in cuprates [1]. Our results suggest that the charge dynamics in hole-doped cuprates are mostly associated with the O sites, highlighting the importance of the three band model in the cuprates [3, 4]. Going beyond, it would be interesting to utilise the site-sensitivity of the RIXS technique to characterise plasmon behaviour in other layered superconductors, like iron-pnictides [31], having strong out-of-plane band dispersions, or the newly-found nickelates in which 2D Ni- $3d$  states strongly hybridise with 3D rare-earth  $5d$  states [32].

## ACKNOWLEDGEMENTS

We thank W.-S. Lee, V. Kresin, J. Lorenzana and S. Johnston for insightful discussions. All data were taken at the I21 RIXS beamline of Diamond Light Source (United Kingdom) using the RIXS spectrometer designed, built and owned by Diamond Light Source. We acknowledge Diamond Light Source for providing the beamtime on Beamline I21 under proposals SP20709 and MM24587. Work at Bristol was supported by EPSRC Grant EP/R011141/1. H. Y. was supported by JSPS KAKENHI Grant No.JP18K18744 and JP20H01856. We acknowledge T. Rice for the technical support throughout the beamtimes. We also thank G. B. G. Stenning and D. W. Nye for help on the Laue instrument in the Materials Characterisation Laboratory at the ISIS Neutron and Muon Source.

## AUTHOR CONTRIBUTIONS

K.-J.Z., S.M.H., and A.N. conceived the project; A.N., K.-J.Z., M.Z., S.M.H., A.N.P., J.L., A.C.W., and M.G.F. performed RIXS measurements on LSCO; A.N., K.-J.Z., and M.G.F. performed RIXS measurements on Bi2201; A.N. analysed the data with support from K.-J.Z., and S.M.H.; H.C.R., M.Z. and S.M.H. prepared and characterised LSCO samples; H.E. and D.S. synthesised and characterised Bi2201 samples; M.B., H.Y., and A.G. performed theoretical calculations; A.N., K.-J.Z., and S.M.H. wrote the manuscript with input from all the authors.

## COMPETING INTERESTS

The authors declare no competing financial interests.

## ADDITIONAL INFORMATION

**Correspondence and requests for materials** should be addressed to A.N., S.M.H., or K.-J.Z.

## I. METHODS

### A. RIXS measurements

High-quality single crystals of  $\text{La}_{1.84}\text{Sr}_{0.16}\text{CuO}_4$  (LSCO) and  $\text{Bi}_2\text{Sr}_{1.6}\text{La}_{0.4}\text{CuO}_{6+\delta}$  (Bi2201) were used to collect the RIXS spectra. Superconducting transition temperatures  $T_c$ s from magnetisation measurements were found to be 38 K and 34.5 K for LSCO and Bi2201 respectively, consistent with optimal hole-doping of  $\sim 0.16$ . Samples were cooled to their respective  $T_c$ s prior to measurement. Lattice constants used for LSCO (Bi2201) are  $a = b = 3.77$  (3.86) Å and  $c = 13.1$  (24.69) Å. See Supplementary Information I for details of sample growth, preparation and characterisation.

RIXS spectra at O  $K$ -edge were collected with an energy resolution of  $\Delta E \simeq 0.043$  eV, at I21-RIXS beam line, Diamond Light Source, United Kingdom [33]. We denote momentum transfers along  $h$ -,  $k$ - and  $l$ -directions in reciprocal lattice units where  $\mathbf{Q} = ha^* + kb^* + lc^*$  ( $a^* = 2\pi/a$ ,  $b^* = 2\pi/b$ ,  $c^* = 2\pi/c$ ),  $k = 0$  if not stated explicitly. Additional spectra were also collected at the Cu  $L_3$ -edge for both the samples with an energy resolution of  $\Delta E \simeq 0.045$  eV. Samples were mounted such that the  $a$ -axis and  $c$ -axis lay in the horizontal scattering plane while the  $b$ -axis was perpendicular to the scattering plane (Fig. 1(d)). To map the dispersion of plasmon excitations in the  $(h, l)$ -plane in RIXS, one needs to continuously change the incident and scattering angles, a newly achieved capability at I21 RIXS beamline, Diamond light source, UK [33]. The O  $K$ -edge XAS shown in Fig. 1(b) were collected in total electron yield mode. All RIXS data presented here were obtained with incident  $\sigma$  polarisation (perpendicular to the scattering plane) to enhance the charge excitations [14]. The zero-energy transfer position and resolution of the RIXS spectra were determined from subsequent measurements of elastic peaks from an adjacent carbon tape.

### B. RIXS data fitting

RIXS data were normalised to the incident photon flux, and subsequently corrected for self-absorption effects using the procedure described in [34] prior to fitting. A Gaussian lineshape with the experimental energy resolution was used to fit the elastic line. Gaussian lineshapes were also used to fit the low energy phonon excitations

at  $\sim 0.045$  eV and their overtones. Anti-symmetrised Lorentzian functions were used to fit the plasmon and the bimagnon peaks (See Supplementary Information III). First we extracted the zone-centre energy, amplitude and width of the broad incoherent mode at  $h = 0.01$  and concluding this to be a bimagnon, fixed its amplitude and width for the whole  $(h, l)$ -range [22, 35]. The energy values of the bimagnons were allowed to vary within  $\pm 20$  meV for the RIXS spectra along  $h$ -direction. For the RIXS spectra along  $l$ -direction, bimagnon energies were kept fixed to the values obtained for corresponding  $h$ -values from the  $h$ -direction scans. This allowed us to decompose the inelastic spectra into two components with less ambiguity, especially for the  $h$ -values where energies of the two modes were nearby. Significant correlations were however found below  $h < 0.02$ , between the elastic,

phonon and plasmon amplitudes and energies, and hence the plasmon energy values determined in these regions are less conclusive. A high energy quadratic background was also included in the fitting model to account for the tailing contribution from  $dd$ -excitations above 1.5 eV. Representative RIXS spectra fits with the different peaks are shown at the top of Fig. 2(e, f), while rest are presented in Supplementary Information III.

### C. $t$ - $J$ - $V$ model

For discussing the nature and origin of three-dimensional charge excitations in LSCO and Bi2201 we employed the minimal layered  $t$ - $J$ - $V$  model [2, 5]:

$$H = - \sum_{i,j,\sigma} t_{ij} \tilde{c}_{i\sigma}^\dagger \tilde{c}_{j\sigma} + \sum_{\langle i,j \rangle} J_{ij} \left( \vec{S}_i \cdot \vec{S}_j - \frac{1}{4} n_i n_j \right) + \frac{1}{2} \sum_{i,j} V_{ij} n_i n_j. \quad (1)$$

See Supplementary Information IV for the details of the hopping parameters  $t_{ij}$  and the exchange parameter  $J_{ij}$  used in the model. The interlayer hopping  $t_z$  was also included in  $t_{ij}$ . The form of long-range Coulomb interaction  $V_{ij}$  used in Eq. 6 in momentum space is [3]:

$$V(\mathbf{Q}) = \frac{V_c}{A(q_x, q_y) - \cos q_z}, \quad (2)$$

where  $V_c = e^2 d (2\epsilon_\perp a^2)^{-1}$  and  $A(q_x, q_y) = \alpha(2 - \cos q_x - \cos q_y) + 1$  with  $\alpha = \frac{\epsilon_\parallel / \epsilon_\perp}{(a/d)^2}$ ,  $e$  the elementary charge and high frequency in- $(\epsilon_\parallel)$  and out-of-plane  $(\epsilon_\perp)$  dielectric constants.

The model Hamiltonian Eq. 6 contains several material dependant parameters. To reduce the number of tuning parameters in the model, we have used, if available, the most common values from literature. The optical plasmon ( $\omega_{\text{opt}}$ ) energy was fixed at 0.85 eV for both LSCO and Bi2201 as reported from optical measurements which are sensitive to only the  $l = 0$  momentum transfers [38–40]. The exchange coupling parameter  $J$  was taken as  $0.3t$  for both the materials given their similar values in the parent compounds [41–43]. It is important to mention

here that plasmons are nearly unaffected by the value of  $J$ . The nearest neighbour hopping parameter  $t/2$  was fixed at 0.35 eV for both the materials [19, 44]. We took the second-nearest neighbour hopping parameter  $t'$ , whose exact value is not known apart from reports that  $|t'_{\text{LSCO}}| < |t'_{\text{Bi2201}}|$ , to be  $-0.2t$  for LSCO and  $-0.35t$  for Bi2201 [5, 21, 44, 45]. We however found that the overall nature of plasmon dispersions does not depend on a precise choice of the band parameters.

We found the optical plasmon energy to be proportional to  $\sqrt{V_c/\alpha}$  of Eq. 2. Depending on the band parameters, we obtained the proportionality constant to be 0.41 for LSCO and 0.40 for Bi2201. With the band parameters fixed, the value of  $V_c/\alpha$  was tuned to get  $\omega_{\text{opt}} = 0.85$  eV. Next,  $V_c$  and  $\alpha$  values were optimised to best match the plasmon dispersions observed in the experiment. For LSCO (Bi2201), we obtained  $V_c$  and  $\alpha$  to be 18.9 eV (52.5 eV) and 3.47 (8.14) respectively. This gave for LSCO (Bi2201),  $\epsilon_\perp$  as  $2.21\epsilon_0$  ( $1.43\epsilon_0$ ) and  $\epsilon_\parallel$  as  $1.62\epsilon_0$  ( $1.14\epsilon_0$ ). Microscopically therefore the relatively large values of  $V_c$  and  $\alpha$  in Bi2201 come mainly from a large interlayer spacing  $d$ . The interlayer hopping  $t_z$  was tuned to match the plasmon energies for  $h \rightarrow 0.0$  and an upper limit of  $0.01t$  was found for both LSCO and Bi2201 (See Supplementary Information Fig. S10).

- 
- [1] Keimer, B., Kivelson, S. A., Norman, M. R., Uchida, S. & Zaanen, J. From quantum matter to high-temperature superconductivity in copper oxides. *Nature* **518**, 179 (2015).
  - [2] Zaanen, J., Sawatzky, G. A. & Allen, J. W. Band gaps and electronic structure of transition-metal compounds, *Phys. Rev. Lett.* **55**, 418 (1985).
  - [3] Emery, V. J. Theory of high- $T_c$  superconductivity in oxides, *Phys. Rev. Lett.* **58**, 2794 (1987).
  - [4] Varma, C. M., Schmitt-Rink S. & Abrahams, E. Charge transfer excitations and superconductivity in “ionic” metals, *Sol. State. Comm.* **62**, 681 (1987).
  - [5] Armitage, N. P., Fournier, P. & Greene, R. L. Progress and perspectives on electron-doped cuprates, *Rev. Mod. Phys.* **82**, 2421 (2010).
  - [6] Chen, C. T. et al. Out-of-plane orbital characters of intrinsic and doped holes in  $\text{La}_{2-x}\text{Sr}_x\text{CuO}_4$ . *Phys. Rev. Lett.* **68**,

- 2543 (1992).
- [7] Comin, R. & Damascelli, A. Resonant X-ray scattering studies of charge order in cuprates. *Ann. Rev. Cond. Mater. Phys.* **7**, 369 (2016).
  - [8] Diaconescu, B. et al. Low-energy acoustic plasmons at metal surfaces. *Nature* **448**, 57 (2007).
  - [9] Fetter, A. Electrodynamics of a layered electron gas. I. Single layer. *Ann. Phys.* **81**, 367 (1973).
  - [10] Fetter, A. L. Electrodynamics of a layered electron gas II. Periodic array. *Ann. Phys.* **88**, 1 (1974).
  - [11] Kresin, V. Z. & Morawitz, H. Layer plasmons and high- $T_c$  superconductivity. *Phys. Rev. B* **37**, 7854 (1988).
  - [12] Greco, A., Yamase, H. & Bejas, M. Origin of high-energy charge excitations observed by resonant inelastic X-ray scattering in cuprate superconductors. *Commun. Phys.* **2**, 3 (2019).
  - [13] Markiewicz, R. S., Hasan, M. Z., & Bansil, A. Acoustic plasmons and doping evolution of Mott physics in resonant inelastic X-ray scattering from cuprate superconductors. *Phys. Rev. B* **77**, 094518 (2008).
  - [14] Hepting, M. et al. Three-dimensional collective charge excitations in electron-doped copper oxide superconductors. *Nature* **563**, 374 (2018).
  - [15] Lin, J. et al. Doping evolution of the charge excitations and electron correlations in electron-doped superconducting  $\text{La}_{2-x}\text{Ce}_x\text{CuO}_4$ . *npj Quantum Mater.* **5**, 4 (2020).
  - [16] Lee, W. et al. Asymmetry of collective excitations in electron- and hole-doped cuprate superconductors. *Nat. Phys.* **10**, 883 (2014).
  - [17] Dellea, G. et al. Spin and charge excitations in artificial hole- and electron-doped infinite layer cuprate superconductors. *Phys. Rev. B* **96**, 115117 (2017).
  - [18] Miao, H. et al. High-temperature charge density wave correlations in  $\text{La}_{1.875}\text{Ba}_{0.125}\text{CuO}_4$  without spincharge locking. *Proc. Natl Acad. Sci. USA* **114**, 12430 (2017).
  - [19] Ishii, K. et al. Observation of momentum-dependent charge excitations in hole-doped cuprates using resonant inelastic X-ray scattering at the oxygen  $K$  edge. *Phys. Rev. B* **96**, 115148 (2017).
  - [20] Mitrano, M. et al. Anomalous density fluctuations in a strange metal. *Proc. Natl. Acad. Sci. USA* **115**, 5392 (2018).
  - [21] Hashimoto, M. et al. Doping evolution of the electronic structure in the single-layer cuprate  $\text{Bi}_2\text{Sr}_{2-x}\text{La}_x\text{CuO}_{6+\delta}$ : comparison with other single-layer cuprates. *Phys. Rev. B* **77**, 094516 (2008).
  - [22] Bisogni, V. et al. Bimagnon studies in cuprates with resonant inelastic X-ray scattering at the O  $K$  edge. II. Doping effect in  $\text{La}_{2-x}\text{Sr}_x\text{CuO}_4$ . *Phys. Rev. B* **85**, 214528 (2012).
  - [23] Minola, M. et al. Crossover from collective to incoherent spin excitations in superconducting cuprates probed by detuned resonant inelastic X-ray scattering. *Phys. Rev. Lett.* **119**, 097001 (2001).
  - [24] Singh, A. et al. Acoustic plasmons and conducting carriers in hole-doped cuprate superconductors. *arXiv:2006.13424v1* (2020).
  - [25] Abbamonte, P. et al. Spatially modulated Mottness in  $\text{La}_{2-x}\text{Ba}_x\text{CuO}_4$ . *Nature Phys.* **1**, 155 (2005).
  - [26] Achkar, A. J. et al. Resonant X-ray scattering measurements of a spatial modulation of the Cu  $3d$  and O  $2p$  energies in stripe-ordered cuprate superconductors. *Phys. Rev. Lett.* **110**, 017001 (2013).
  - [27] Li, J. et al. Multi-orbital charge density wave excitations and concomitant phonon anomalies in  $\text{Bi}_2\text{Sr}_2\text{LaCuO}_{6+\delta}$ . *Proc. Natl. Acad. Sci. USA*, (2020).
  - [28] Johannes, M. D. & Mazin, I. I. Fermi surface nesting and the origin of charge density waves in metals, *Phys. Rev. B* **77**, 165135 (2008).
  - [29] Forgan, E. M. et al., The microscopic structure of charge density waves in underdoped  $\text{YBa}_2\text{Cu}_3\text{O}_{6.54}$  revealed by X-ray diffraction, *Nat. Comms.* **6**, 10064 (2015).
  - [30] Fink, J. et al. Charge ordering in  $\text{La}_{1.8-x}\text{Eu}_{0.2}\text{Sr}_x\text{CuO}_4$  studied by resonant soft X-ray diffraction. *Phys. Rev. B* **79**, 100502(R) (2009).
  - [31] Paglione, J. & Greene, R. L. High-temperature superconductivity in iron-based materials. *Nat. Phys.* **6**, 645 (2010).
  - [32] Hepting, M. et al. Electronic structure of the parent compound of superconducting infinite-layer nickelates. *Nat. Mater.* **19**, 381 (2020).
  - [33] <https://www.diamond.ac.uk/Instruments/Magnetic-Materials/I21.html>
  - [34] Minola, M. et al. Collective Nature of Spin Excitations in Superconducting Cuprates Probed by Resonant Inelastic X-Ray Scattering. *Phys. Rev. Lett.* **114**, 217003 (2015).
  - [35] Vernay, F. H., Gingras, M. J. P. & Devereaux, T. P. Momentum-dependent light scattering in insulating cuprates. *Phys. Rev. B* **75**, 020403(R) (2007).
  - [36] Zhang, F. C. & Rice, T. M. Effective Hamiltonian for the superconducting Cu oxides. *Phys. Rev. B* **37**, 3759 (1988).
  - [37] Becca, F., Tarquini, M., Grilli, M. & Di Castro, C. Charge-density waves and superconductivity as an alternative to phase separation in the infinite-U Hubbard-Holstein model. *Phys. Rev. B* **54**, 12443 (1996).
  - [38] van Heumen, E., Meevasanam W., Kuzmenko, A. B., Eisaki, H. & van der Marel, D. Doping-dependent optical properties of  $\text{Bi2201}$ . *New J. Phys.* **11**, 055067 (2009).
  - [39] Uchida, S. et al. Optical spectra of  $\text{La}_{2-x}\text{Sr}_x\text{CuO}_4$ : Effect of carrier doping on the electronic structure of the  $\text{CuO}_2$  plane. *Phys. Rev. B* **43**, 7942 (1991).
  - [40] Suzuki, M. Hall coefficients and optical properties of  $\text{La}_{2-x}\text{Sr}_x\text{CuO}_4$  single-crystal thin films. *Phys. Rev. B* **39**, 2312 (1989).
  - [41] Hybertsen, M. S., Stechel, E. B., Schluter, M. & Jennison, D. R. Renormalization from density-functional theory to strong-coupling models for electronic states in Cu-O materials. *Phys. Rev. B* **41**, 11068 (1990).
  - [42] Peng, Y. Y. et al. Influence of apical oxygen on the extent of in-plane exchange interaction in cuprate superconductors. *Nat. Phys.* **13**, 1201 (2017).
  - [43] Lee, P. A., Nagaosa, N. & Wen, X.-G. Doping a Mott insulator: physics of high-temperature superconductivity. *Rev. Mod. Phys.* **78**, 17 (2006).
  - [44] Horio, M. et al. Three-dimensional Fermi surface of overdoped La-based cuprates. *Phys. Rev. Lett.* **121**, 077004 (2018).
  - [45] Pavarini, E., Dasgupta, I., Saha-Dasgupta, T., Jepsen, O. & Andersen O. K. Band-structure trend in hole-doped cuprates and correlation with  $T_{c\text{max}}$ . *Phys. Rev. Lett.* **87**, 047003 (2001).

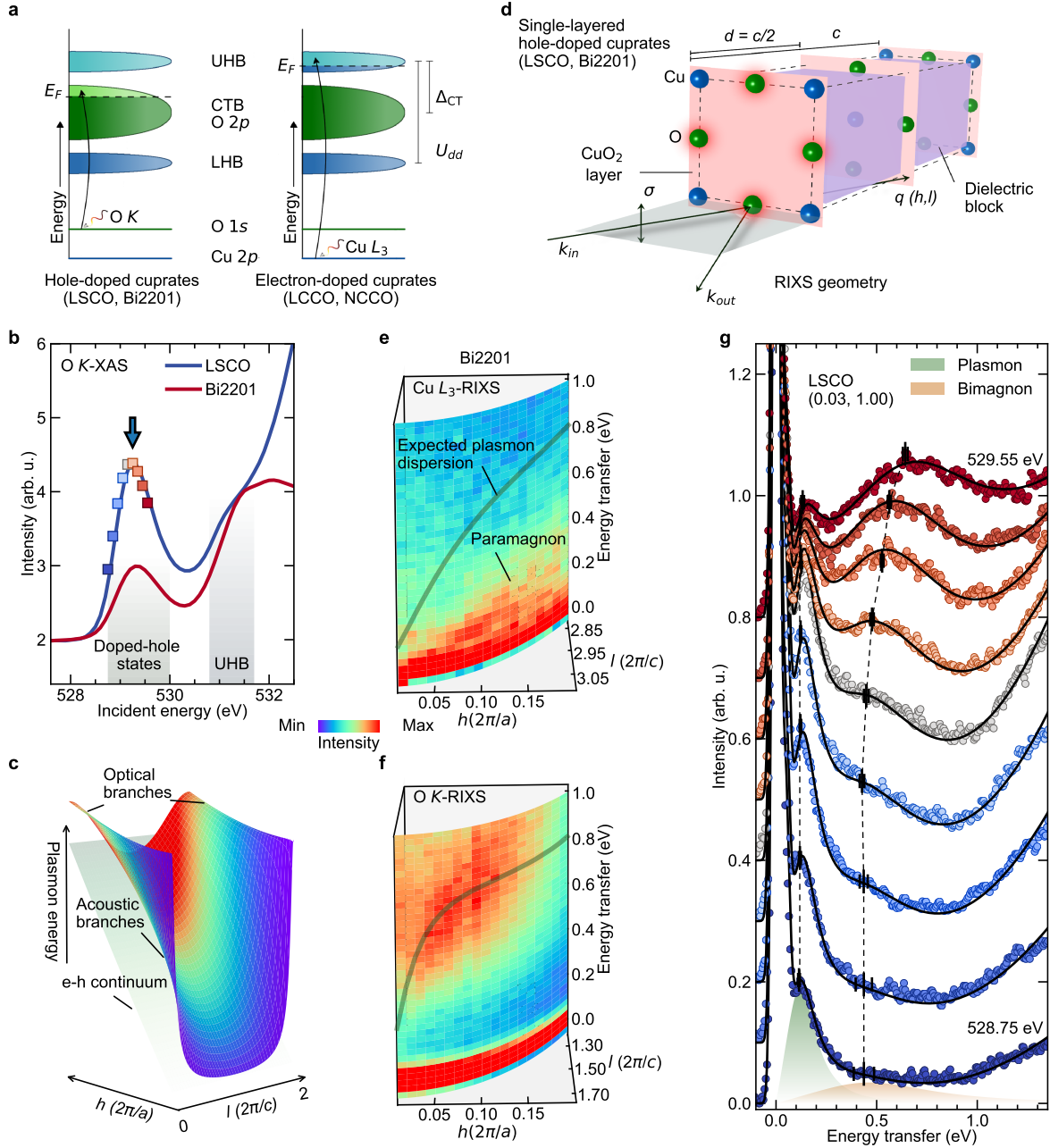


**FIG. 1. Probing plasmons in hole-doped cuprates using RIXS.** **a**, Schematic electronic structure of cuprates in the Zaanen-Sawatzky-Allen scheme [2–5]. Holes are doped into the charge transfer band and electrons are doped into the upper Hubbard band. Vertical arrows represent the principal excitation processes occurring at the O  $K$ - and Cu  $L_3$ -XAS peaks. **b**, Peak feature attributed to the doped-holes observed through O  $K$ -XAS for the two systems [6]. The arrow shows the incident energy chosen to probe the plasmon dispersions in this work. **c**, Acoustic plasmon branches dispersing towards zero-energy in the  $h$ -direction while maintaining a periodicity of  $l = 2$  in the  $l$ -direction, due to the presence of a  $\text{CuO}_2$  layer in the middle of a unit cell in single-layered systems. **d**, Representative unit cell of single-layered high- $T_c$  cuprates, and the RIXS scattering geometry showing incoming ( $k_{in}$ ) and scattered ( $k_{out}$ ) X-ray beams. **e** and **f**, RIXS intensity maps for Bi2201 at a fixed scattering angle of  $114^\circ$  at Cu  $L_3$ - and O  $K$ -edges respectively. **f**, Incident energy detuned, vertically stacked RIXS spectra, showing their decomposition into a sharp Raman-like peak and a broad energy-shifting peak for LSCO at  $(h = 0.03, l = 1.00)$ . Colours of the spectra correspond to incident energies shown in **b**. Solid black lines are fits to the RIXS spectra (see Methods B and Supplementary Information III). Vertical black bars are least-square-fit peak positions.

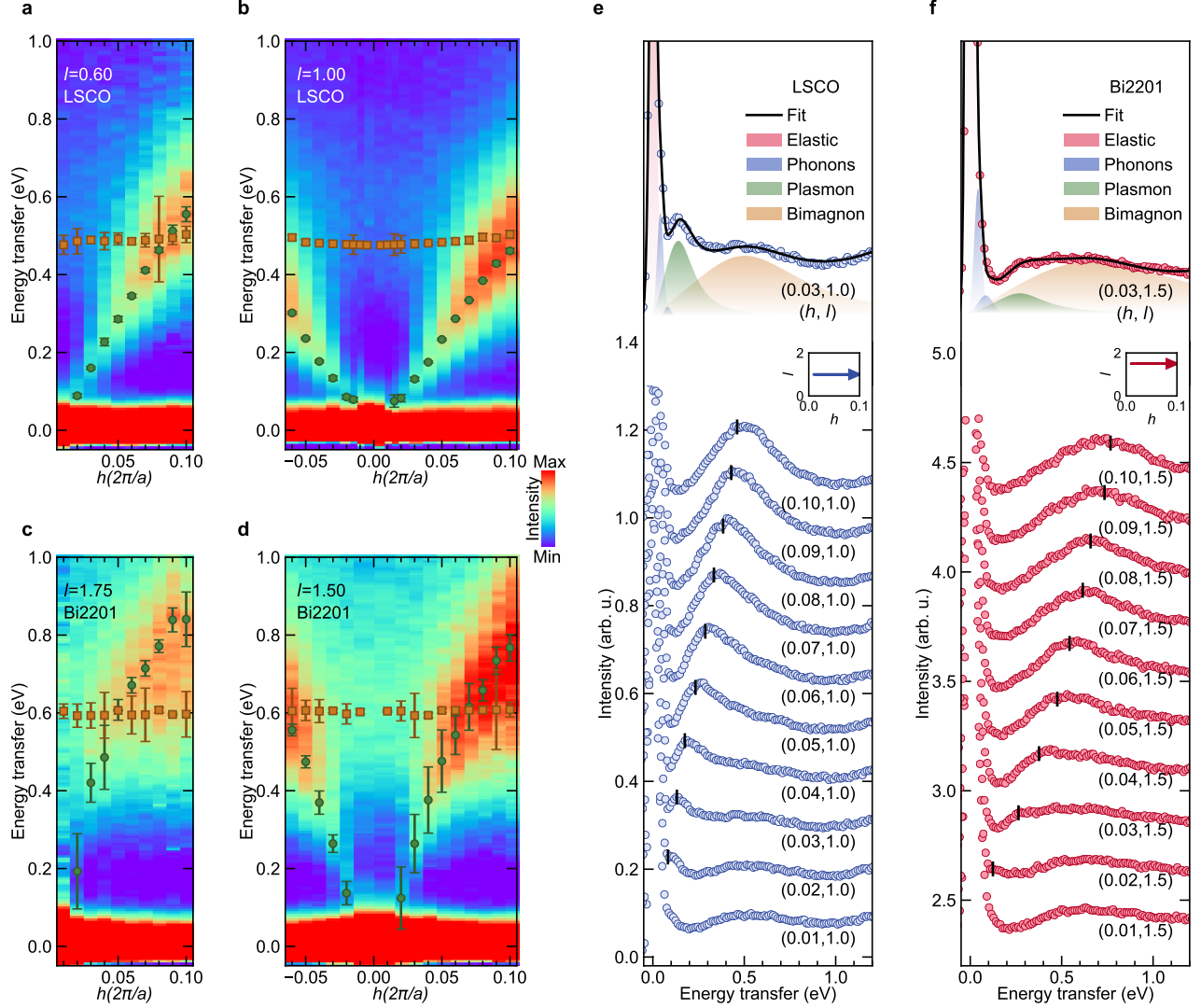


FIG. 2. **In-plane plasmon dispersions in LSCO and Bi2201.** RIXS intensity maps of **a, b**, LSCO for momentum transfer along the  $h$ -direction at  $l = 0.60$  and  $l = 1.00$  and **c, d**, of Bi2201 at  $l = 1.75$  and  $l = 1.50$ . Green circle symbols indicate the least-square-fit peak positions of the plasmon excitations. Brown square symbols show the fitted bimagnon peak positions. **e, f**, Top, representative RIXS spectra (blue and red circle symbols) at mentioned  $(h, l)$ -values for LSCO and Bi2201. Shaded areas represent the different peak profiles in the energy transfer region below 1.5 eV. Black solid lines are fits to the RIXS spectra. See Methods B for details of the decomposition procedure. **e, f**, Bottom, vertically stacked RIXS spectra at indicated  $(h, l)$ -values. Vertical black bars are least-square-fit plasmon peak positions. The insets indicate the directions in the  $h, l$ -plane, along which the shown RIXS spectra have been collected.



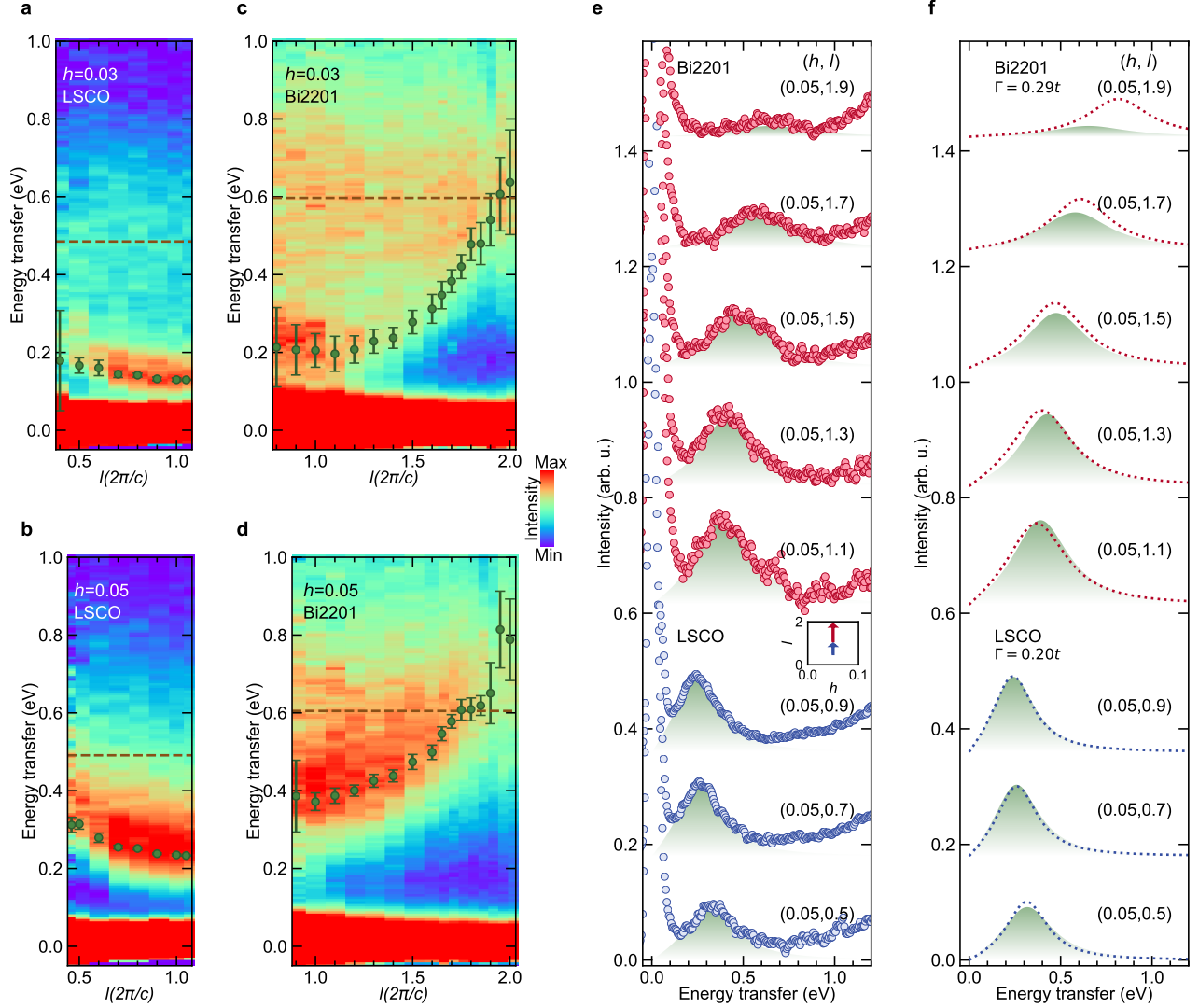


FIG. 3. **Out-of-plane plasmon dispersions in LSCO and Bi2201.** RIXS intensity maps of **a**, **b**, LSCO and of **c**, **d**, Bi2201 for momentum transfer along the  $l$ -direction at  $h = 0.03$  and  $h = 0.05$ . Green circle symbols indicate the least-square-fit peak positions of the plasmons. Brown dashed line shows the extracted bimagnon energies from the  $h$ -direction scans. **e**, Representative RIXS spectra at mentioned  $(h, l)$ -values for LSCO (blue circle symbols) and Bi2201 (red circle symbols). From the RIXS spectra, fitted peak profiles from bimagnons have been subtracted to show the evolution of the plasmon peak (green shaded area). The inset indicates the direction in the  $(h, l)$ -plane, along which the shown RIXS spectra have been collected. **f**,  $\chi''_c(\mathbf{Q}, \omega)$  calculated from  $t$ - $J$ - $V$  model for corresponding  $(h, l)$ -values in **e** for LSCO (Bi2201) are shown by the dotted blue (red) lines. Shaded green areas are the plasmon peak profiles obtained from RIXS data fitting. Different broadening factors ( $\Gamma = 0.29t$  for Bi2201 and  $0.2t$  for LSCO) were chosen to replicate the lineshapes of the two materials.



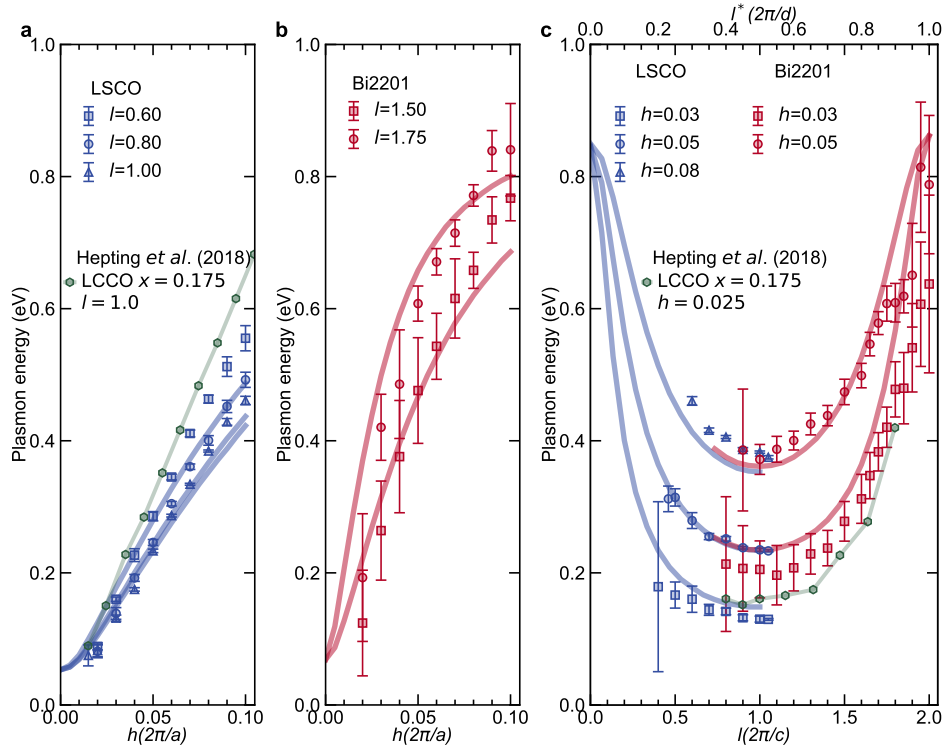


FIG. 4. **Comparison of plasmon dispersions obtained from RIXS with  $t$ - $J$ - $V$  model LSCO and Bi2201.** **a, b,** Plasmon energies in LSCO (blue symbols) and Bi2201 (red symbols) for momentum transfer along the  $h$ -direction for different  $l$ -values and **c,** for momentum transfer along the  $l$ -direction for different  $h$ -values, summarised from least-square-fits of RIXS spectra. Continuous lines are plasmon dispersions obtained from optimised  $t$ - $J$ - $V$  model. Also compared are the plasmon dispersions from electron-doped  $\text{La}_{2-x}\text{Ce}_x\text{CuO}_4$  ( $x=0.175$ ) (green lines with symbols) [14].

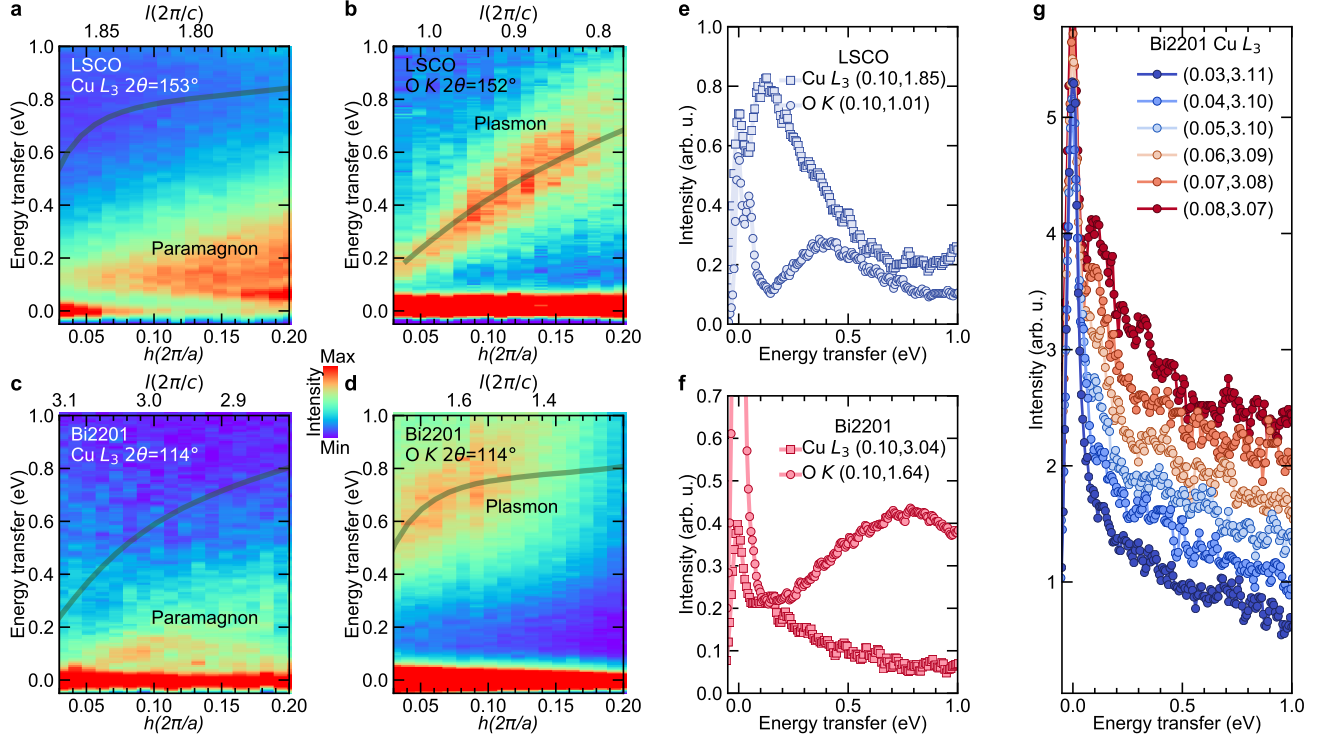


FIG. Extended Fig. 1. **Comparison of Cu  $L_3$ - and O  $K$ -RIXS for probing plasmons in LSCO and Bi2201.** **a, b,** RIXS intensity maps of LSCO for momentum transfer along the  $h$ -direction and **c, d,** of Bi2201 at Cu  $L_3$  absorption and O  $K$  hole-peaks. The spectra are collected with a fixed scattering angle ( $2\theta$ ) for each map and hence the  $(h, l)$ -values vary simultaneously. Green solid lines show the expected plasmon dispersions from  $t$ - $J$ - $V$  model. **e, f,** Representative RIXS spectra for LSCO and Bi2201 at given  $(h, l)$ -values for Cu  $L_3$ - (square symbols) and O  $K$ - (circle symbols) edges. **g,** RIXS spectra for Bi2201 at given  $(h, l)$ -values for Cu  $L_3$ -edge.

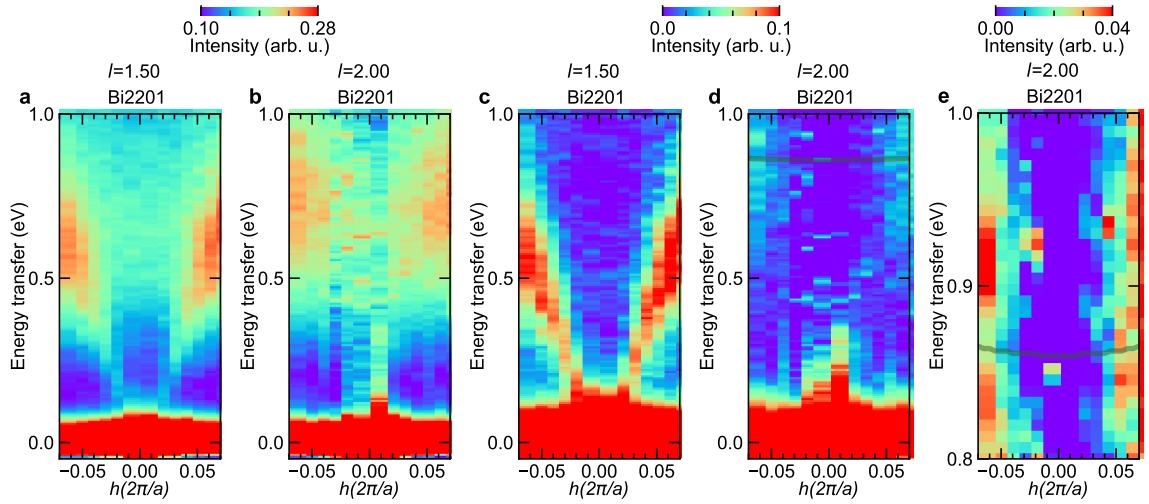


FIG. Extended Fig. 2. **Optical plasmon dispersions in Bi2201.** **a, b,** RIXS intensity maps of Bi2201 for momentum transfer along the  $h$ -direction at  $l = 1.50$  and  $l = 2.00$ . **c, d,** RIXS intensity maps of Bi2201 after subtraction of bimagnon excitations from **a** and **b**. **e,** Zoomed in map of **d**. Continuous line in **d, e,** are the expected optical plasmon dispersion. For both  $h$  close to 0 and  $l$  close to 2 the plasmon amplitudes reduce substantially (see Extended Data Fig. 3). Although some residual spectral weight is visible for slightly higher  $h$ -values at  $l = 2.00$ , the optical plasmon branch still remains intangible.

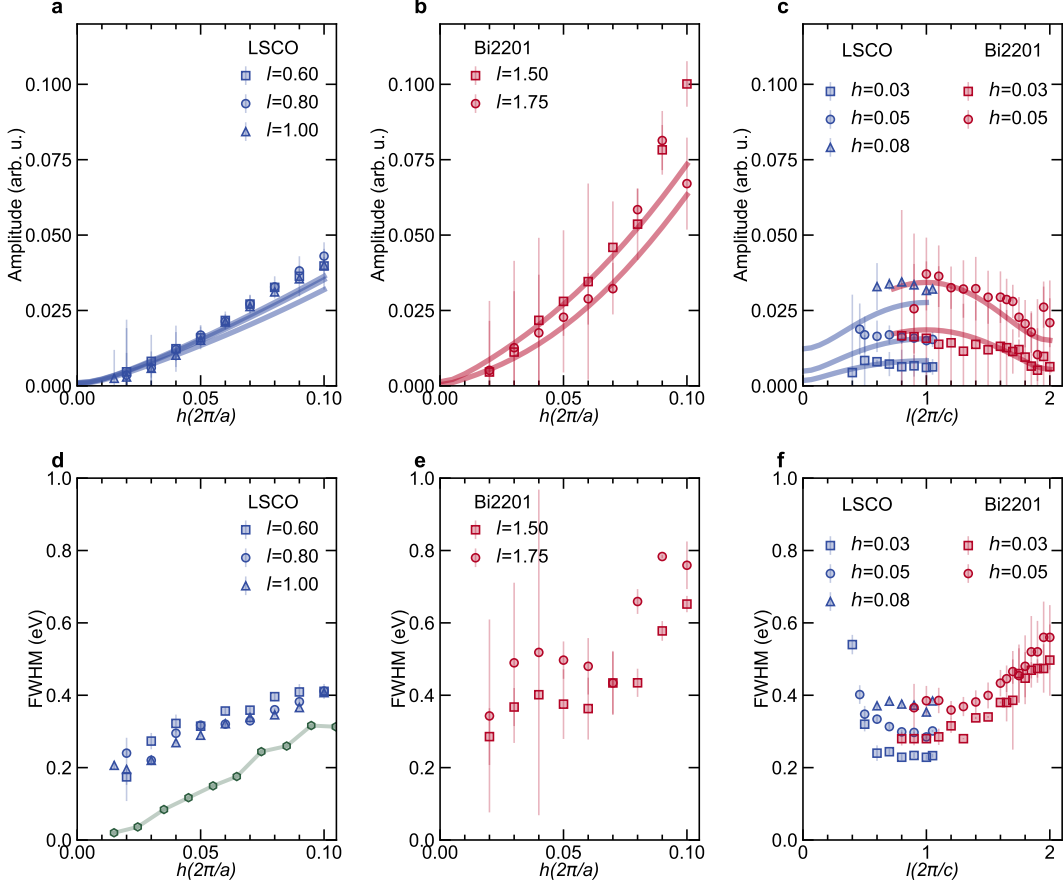


FIG. Extended Fig. 3. **Plasmon amplitude and width variation along  $h$ - and  $l$ -directions in LSCO and Bi2201.** **a**, **b**, and **d**, **e**, Plasmon amplitudes and widths in LSCO (blue symbols) and Bi2201 (red symbols) for momentum transfer along the  $h$ -direction for different  $l$ -values and **c**, and **f**, for momentum transfer along the  $l$ -direction for different  $h$ -values, summarised from least-square-fits of RIXS spectra. Continuous lines are integrated spectral weights of  $\chi_c''(\mathbf{Q}, \omega)$  calculated within the  $t$ - $J$ - $V$  model. To make an appropriate comparison, all the calculated amplitude values were scaled to the experimental values at  $h = 0.05, l = 1.00$  for LSCO and  $h = 0.05, l = 1.50$  for Bi2201. Also compared are the plasmon widths from electron-doped  $\text{La}_{2-x}\text{Ce}_x\text{CuO}_4$  ( $x=0.175$ ) (green line with symbols) [14].

# Supplementary information for the nature of plasmon excitations in hole-doped cuprate superconductors

## I. SAMPLE GROWTH, PREPARATION AND CHARACTERISATION.

High-quality single crystals of  $\text{La}_{1.84}\text{Sr}_{0.16}\text{CuO}_4$  (LSCO) and  $\text{Bi}_2\text{Sr}_{1.6}\text{La}_{0.4}\text{CuO}_{6+\delta}$  (Bi2201) were grown by floating-zone method. Bi2201 sample was annealed at  $650^\circ\text{C}$  in  $\text{O}_2$  atmosphere for two days to improve sample homogeneity. Fig. 1(a) and (b) show the Laue diffraction patterns obtained from LSCO and Bi2201 respectively, for preliminary orientation. The orientations were further refined using in-situ diffraction, charge-order and superstructure (present in Bi2201 due to structural distortions in Bi-O layers) peaks prior to the collection of RIXS spectra. Superconducting transition temperatures  $T_c$ s extracted from magnetisation measurements of LSCO (38 K) and Bi2201 (34.5 K) are shown in Fig. 1(c) and (d). While LSCO was cleaved in vacuum, Bi2201 was cleaved in air and immediately transferred to vacuum. LSCO and Bi2201 samples were cooled down to their respective  $T_c$ s prior to measurement and the pressure inside the sample vessel was maintained at  $\sim 5 \times 10^{-10}$  mbar. Negative and positive values of  $h$  in the RIXS maps presented in this work represent the grazing-incident and grazing-exit geometries respectively (Fig. 1(e,f)). Fig. 1(g) shows the accessible  $(h, l)$ -values at  $0\text{ K}$ -for LSCO and Bi2201 at I21. For each material, reduction in  $l$ -value forces transition from a backward to forward scattering experimental geometry which enhances the elastic line, thereby limiting the lowest usable  $l$ -to study plasmons.

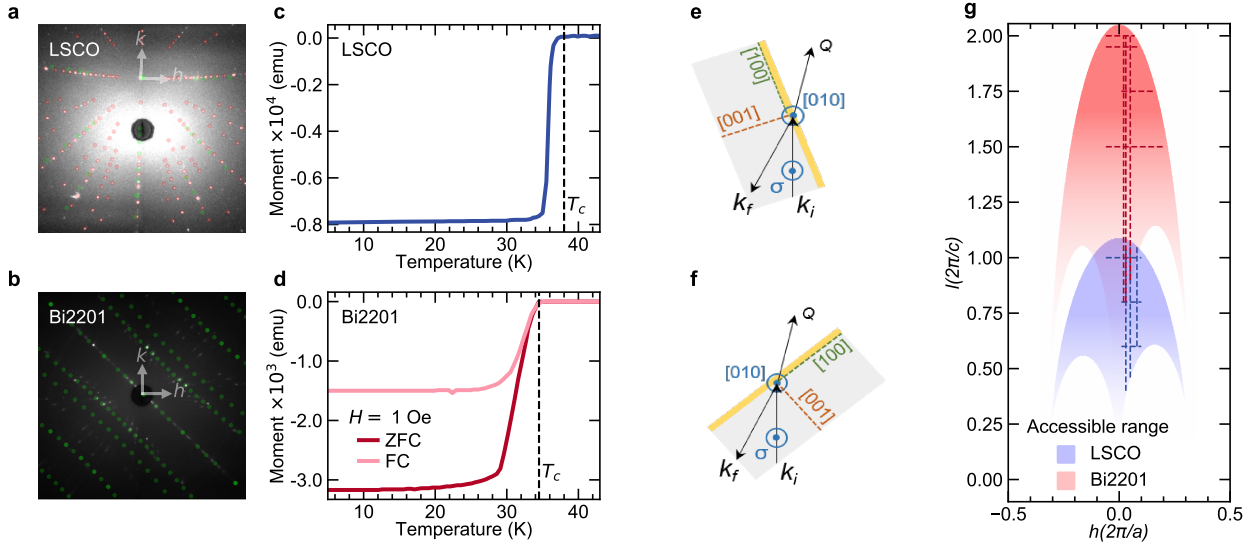


FIG. 1. **Sample properties.** **a, b**, Laue diffraction patterns of LSCO and Bi2201 samples. **c, d**, Zero-Field-Cooled (ZFC) and Field-Cooled (FC) magnetisation curves for LSCO and Bi2201. The onset of the superconducting transition  $T_c$  is shown by the vertical dotted lines. **e**, Grazing-incident and **f**, grazing-exit scattering geometries. **g**, Shows the accessible  $(h, l)$ -values at  $0\text{ K}$ -for LSCO and Bi2201 at I21. Negative and positive values of  $h$  represent the grazing-in and grazing-exit configurations respectively. Vertical and horizontal lines show the  $(h, l)$ -trajectories along which RIXS spectra were collected in this work.

## II. ADDITIONAL RIXS DATA

RIXS intensity map of LSCO for momentum transfer along the  $h$ -direction at  $l = 0.80$  is shown in Fig. 2(a). The plasmon energies from these scans have been used in Fig. 4(a) of the main paper. Extended  $h$ -scans are shown in Fig. 2(b, c) till  $h = 0.15$ , showing the continuous rise of the plasmon energies towards the  $dd$  excitations in Bi2201. RIXS intensity map of LSCO for momentum transfer along the  $l$ -direction at  $h = 0.08$  is shown in Fig. 3(a). The plasmon energies from these scans have been used in Fig. 4(c) of the main paper. In Fig. 3(b) RIXS intensity map of Bi2201 for momentum transfer along the  $l$ -direction at  $h = 0.02$  is shown. Although plasmon dispersion is visible for  $h = 0.02$  in Bi2201, the energies could not be extracted by fitting the data, due to either proximity to elastic line below  $l = 1.5$  or weak spectral weight above  $l = 1.5$ . The over-plotted continuous dispersion line obtained from  $t$ - $J$ - $V$  model seemingly follows the plasmon spectral weight. Plasmon excitations are also observed along the  $k$  directions in

LSCO (see Fig. 4(a)) as expected from the 4-fold symmetry of orbitals in the  $\text{CuO}_2$  planes. As such, using the same parameters of the  $t$ - $J$ - $V$  model optimised for plasmon dispersions along  $h$ - and  $l$ -directions, the plasmon excitations along the  $k$  direction can be reproduced (see Fig. 4(b)).

Close to the zone-centre, high energy-resolution scans are need to differentiate the plasmon peak from the elastic and the phonon peaks. This is important if one wants to study the validity of the  $t$ - $J$ - $V$  model with interlayer hopping which predicts a zone-centre gap for the acoustic plasmons. From the current results we can only estimate the upper limit of the acoustic plasmon energies at the zone-centre to be  $\approx 0.075$  eV for LSCO, setting interlayer hopping  $t_z \lesssim 0.007$  eV in this material (see Fig. 10).

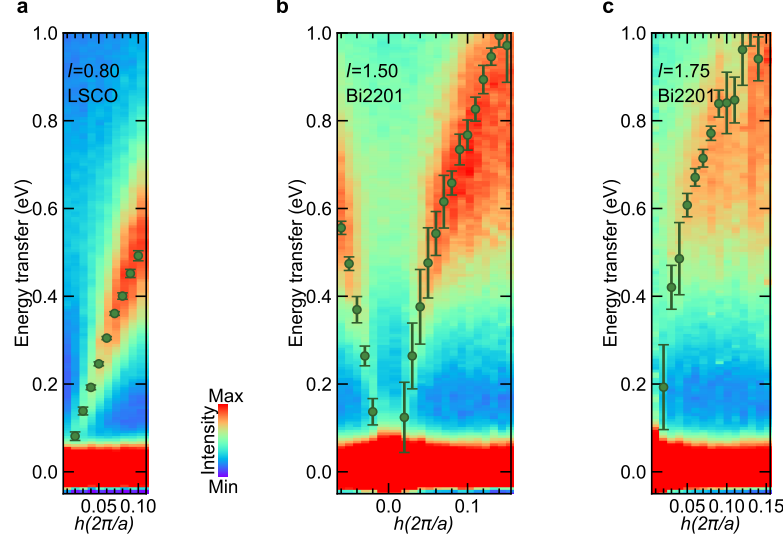


FIG. 2. **Additional in-plane plasmon dispersions in LSCO and Bi2201.** **a**, RIXS intensity map of LSCO for momentum transfer along the  $h$  direction at  $l = 0.80$  and **b**, **c**, of Bi2201 at  $l = 1.50$  and  $l = 1.75$ . Green circle symbols indicate the least-square-fit peak positions of the plasmon excitations. Fitted plasmon energies for LSCO have been used in Fig. 4(a) of the main paper.

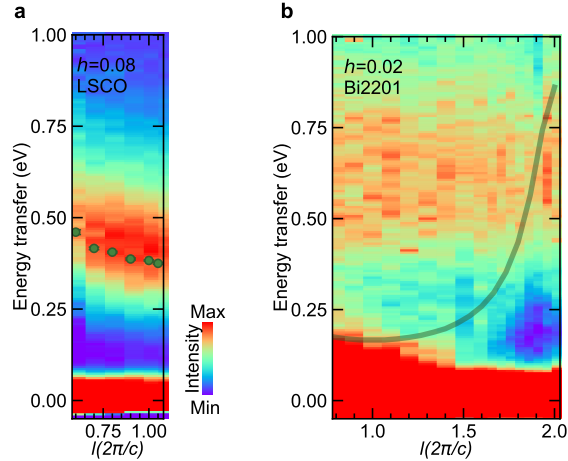


FIG. 3. **Additional out-of-plane plasmon dispersions in LSCO and Bi2201.** **a**, RIXS intensity map of LSCO for momentum transfer along the  $l$ -direction at  $h = 0.80$  and **b**, of Bi2201 at  $h = 0.02$ . Green circle symbols indicate the least-square-fit peak positions of the plasmon excitations. Error bars are smaller than the symbols. Continuous line shows the expected plasmon dispersion from  $t$ - $J$ - $V$  model.

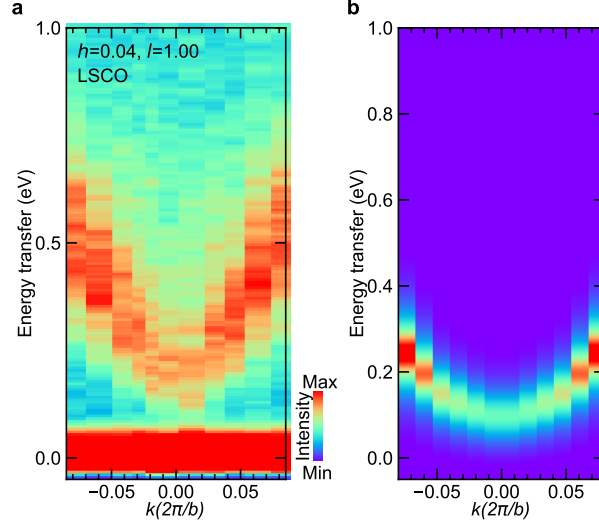


FIG. 4. **Plasmon dispersion in LSCO along  $k$ -direction.** **a**, RIXS intensity map of LSCO for momentum transfer along the  $k$  direction at  $(h = 0.04, l = 1.0)$ . **b**, Intensity map of the charge susceptibility corresponding to the spectra shown in **a**, calculated using  $t$ - $J$ - $V$  model.

### III. RIXS DATA FITTING

All RIXS data shown in this paper were fitted following the procedure described in Methods B. The RIXS spectra fits of LSCO for incident energy detuned scans are shown in Fig. 5. Also in Fig. 5(b) are shown the change in plasmon and bimagnon amplitudes and widths as the incident energy is varied. The non-resonant behaviour of the bimagnon amplitude implies an incoherent character in sharp contrast to the plasmon. RIXS spectra fits of LSCO and Bi2201 for momentum transfer along the  $h$ -direction are shown in Fig. 6 and 7, and along the  $l$ -direction in Fig. 8 and 9 respectively. The scattering intensities  $S(\mathbf{Q}, \omega)$  of the plasmons and bimagnons at given values of  $\mathbf{Q} = ha^* + kb^* + lc^*$  ( $a^* = 2\pi/a$ ,  $b^* = 2\pi/b$ ,  $c^* = 2\pi/c$ ), dependent on the imaginary part of their respective dynamic susceptibilities  $\chi''(\mathbf{Q}, \omega)$  were modelled as:

$$S(\mathbf{Q}, \omega) \propto \frac{\chi''(\mathbf{Q}, \omega)}{1 - e^{-\hbar\omega/k_B T}}, \quad (3)$$

where  $k_B$ ,  $T$  and  $\hbar$  are the Boltzmann constant, temperature and the reduced Planck constant. A generic damped harmonic oscillator model can be used for the response function

$$\chi''(\mathbf{Q}, \omega) \propto \frac{\gamma\omega}{[\omega^2 - \omega_0^2]^2 + 4\omega^2\gamma^2}, \quad (4)$$

where  $\omega_0$  and  $\gamma$  are the undamped frequency and the damping factor respectively. Eq. 4 can be equivalently written using an anti-symmetrised Lorentzian function,

$$\frac{1}{\omega_p} \left[ \frac{\gamma}{(\omega - \omega_p)^2 + \gamma^2} - \frac{\gamma}{(\omega + \omega_p)^2 + \gamma^2} \right], \quad (5)$$

with peaks at  $\pm\omega_p$  for  $\omega_p^2 = \omega_0^2 - \gamma^2$ , given that  $\gamma \leq \omega_0$ , which was found to hold for the plasmon excitations observed in this study (see Extended Data Fig. 3). In the results, we plotted the plasmon propagation energy as the peak  $\omega_p$  of this function.

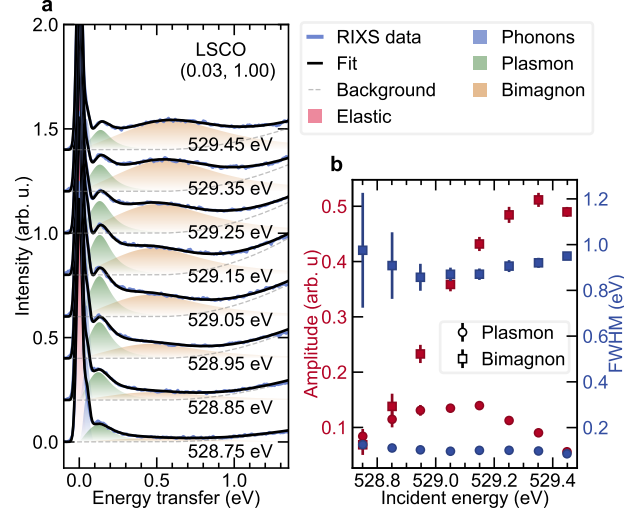


FIG. 5. **RIXS spectra fits of LSCO for varying incident energies.** **a**, Fits to the RIXS spectra of LSCO at ( $h = 0.03$ ,  $l = 1.00$ ) for mentioned incident energies about the *hole*-peak in O *K*-edge XAS presented in Fig. 1(b) of main paper are shown by using the model described in Section III. The extracted plasmon and bimagnon peak energies have been used in Fig. 1(g) of main paper. **b**, The plasmon and bimagnon amplitudes (circle and square red symbols) and widths (circle and square blue symbols) as a variation of incident energy is plotted.

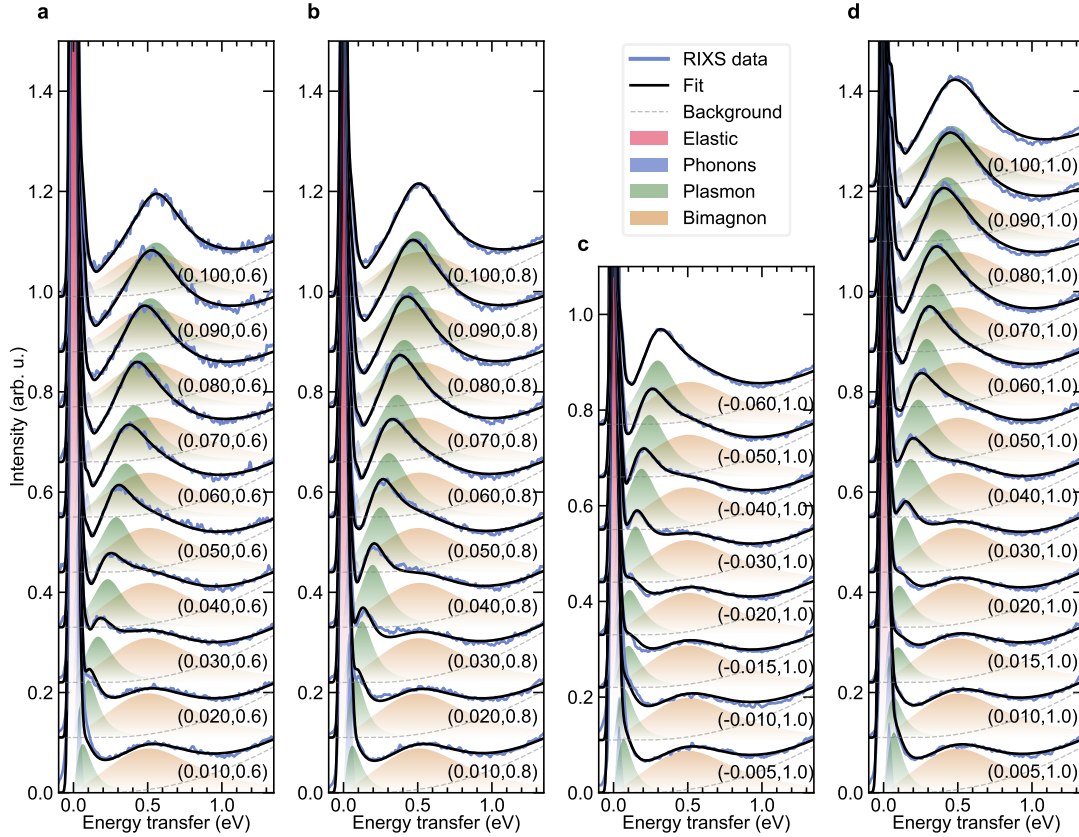


FIG. 6. **RIXS spectra fits of LSCO for momentum transfer along the  $h$  direction.** **a**, **b**, **c**, and **d**, Fits to the RIXS spectra of LSCO presented in Fig. 2 (a, b, e) of main paper at mentioned ( $h$ ,  $l$ )-values are shown by using the model described in Section III. The extracted plasmon peak energies have been used in Fig. 2(a, b, e) and Fig. 4(a) in the main paper and Fig. 2. The plasmon amplitudes and widths have been used in Extended Data Fig. 3 (a, d) of the main paper.



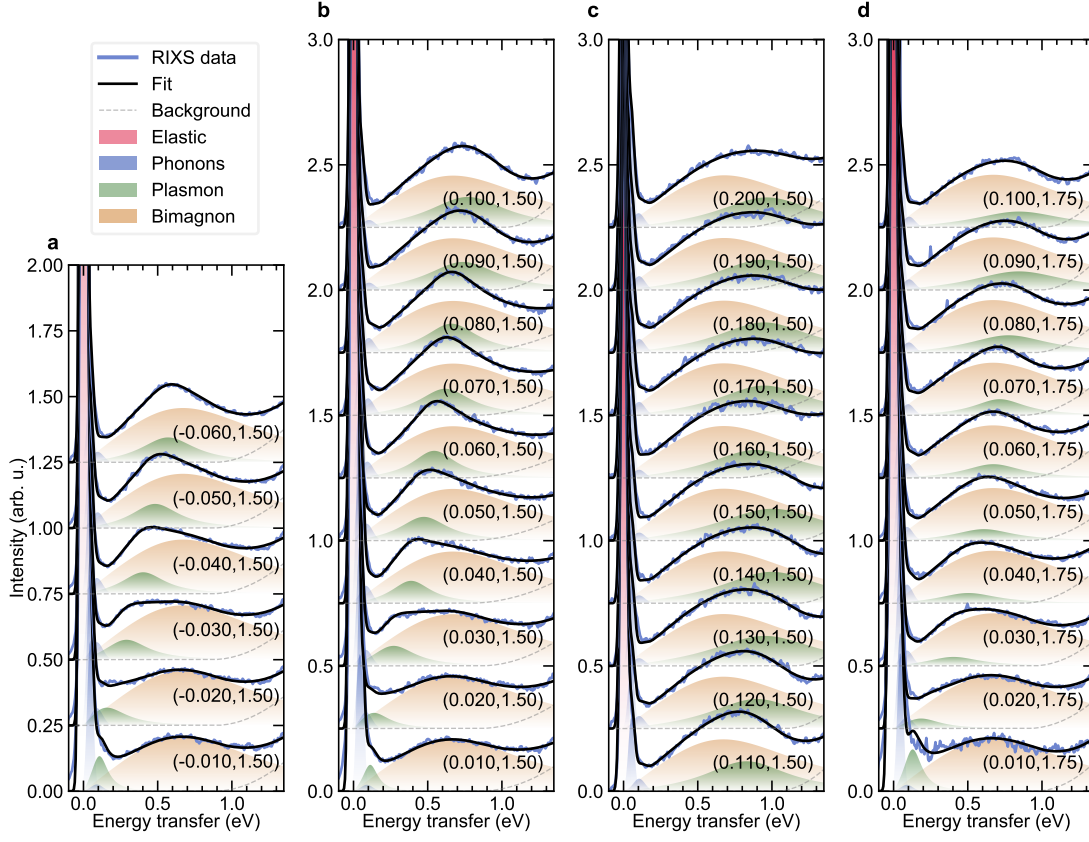


FIG. 7. **RIXS spectra fits of Bi2201 for momentum transfer along the  $h$  direction.** **a**, **b**, **c**, and **d**, Fits to the RIXS spectra of Bi2201 presented in Fig. 2 (c, d, f) of main paper at mentioned  $(h, l)$ -values are shown by using the model described in Section III. The extracted plasmon peak energies have been used in Fig. 2(c, d, f) and Fig. 4(b) in the main paper and Fig. 2. The plasmon amplitudes and widths have been used in Extended Data Fig. 3 (b, e) of the main paper.

#### IV. $t$ - $J$ - $V$ MODEL

We used the following form of the layered  $t$ - $J$ - $V$  model [1]:

$$H = - \sum_{i,j,\sigma} t_{ij} \tilde{c}_{i\sigma}^\dagger \tilde{c}_{j\sigma} + \sum_{\langle i,j \rangle} J_{ij} \left( \vec{S}_i \cdot \vec{S}_j - \frac{1}{4} n_i n_j \right) + \frac{1}{2} \sum_{i,j} V_{ij} n_i n_j. \quad (6)$$

On each plane the hopping  $t_{ij}$  takes a value  $t$  ( $t'$ ) between the first (second) nearest-neighbours sites on the square lattice and  $J$  is the exchange interaction between the nearest-neighbours. Since hole-doped cuprates are correlated electron systems the  $t$ - $J$  model is believed to be a minimal model of the  $\text{CuO}_2$  planes [2]. The fact that we deal with a correlated system is contained in  $\tilde{c}_{i\sigma}^\dagger$  and  $\tilde{c}_{i\sigma}$  which are the creation and annihilation operators, respectively, of electrons with spin  $\sigma$  ( $=\uparrow, \downarrow$ ) in the Fock space without any double occupancy.  $n_i$  is the electron density operator and  $\vec{S}_i$  the spin operator. The three-dimensional nature of the model is considered by the presence of a hopping  $t_z$  between the adjacent planes, and the long-range Coulomb interaction  $V_{ij}$  for a layered system. The form of  $V_{ij}$  in Eq. 6 in momentum space is given in Eq. 2 of main paper [3]. The exchange interaction  $J$  is considered only inside the plane. The out-of-plane exchange term is much smaller than  $J$  [4]. Finally, the indices  $i$  and  $j$  run over the sites of a three-dimensional lattice, and  $\langle i, j \rangle$  indicates a pair of nearest-neighbour sites.

A theoretical treatment of this model is non-trivial because the Hamiltonian is defined in the restricted Hilbert space that prohibits non-double occupancy on each site, which complicate the commutation rules of the operators. In addition, there is no small parameter for perturbation. We implement a large- $N$  expansion [1, 5, 6] where the spin index  $\sigma$  is extended to a new index  $p$  running from 1 to  $N$ . In order to get a finite theory in the limit  $N \rightarrow \infty$ , we rescale the hopping  $t_{ij}$  to  $t_{ij}/N$ ,  $J$  to  $J/N$  and  $V_{ij}$  to  $V_{ij}/N$ , and  $1/N$  is used as the small parameter to control the expansion.  $N$  is put to  $N = 2$  in the end. Although the physical value is  $N = 2$ , the large- $N$  expansion has

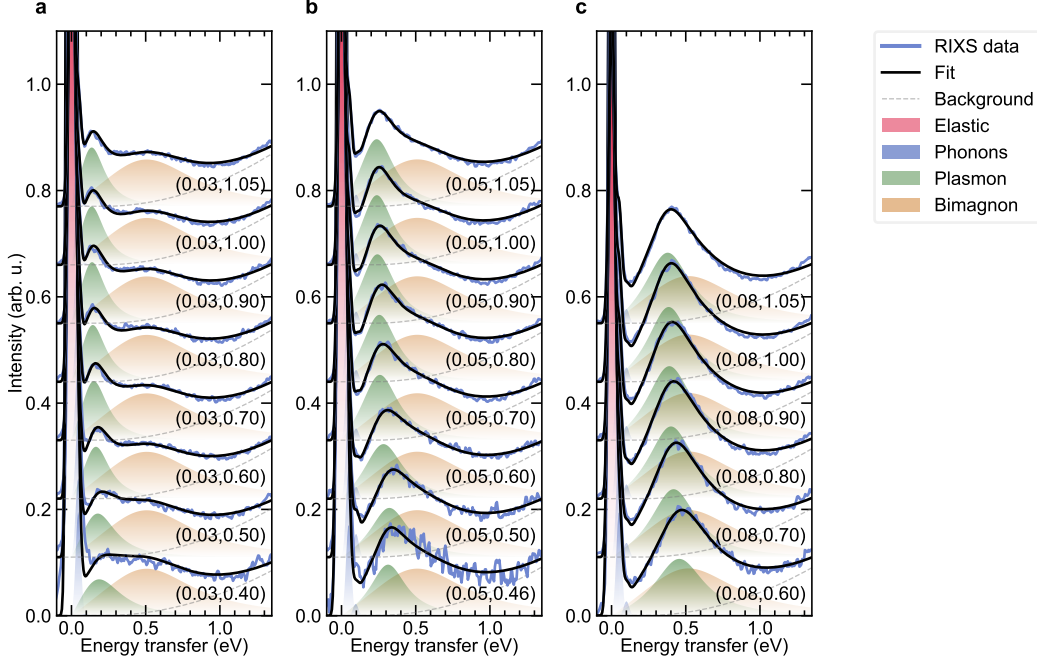


FIG. 8. **RIXS spectra fits of LSCO for momentum transfer along the  $l$ -direction.** **a**, **b**, and **c**, Fits to the RIXS spectra of LSCO presented in Fig. 3 (a, b) of main paper at mentioned  $(h, l)$ -values are shown by using the model described in Section III. The extracted plasmon peak energies have been used in Fig. 3(a, b) and Fig. 4(c) in the main paper and Fig. 3. In Fig. 3(e) of the main paper, RIXS spectra subtracted by the fitted bimagnon contribution have been shown. The plasmon amplitudes and widths have been used in Extended Data Fig. 3 (c, f) of the main paper.

several advantages over usual perturbations theories. Applying the large- $N$  treatment [1] the quasiparticles disperse in momentum space as

$$\epsilon_{\mathbf{k}} = \epsilon_{\mathbf{k}}^{\parallel} + \epsilon_{\mathbf{k}}^{\perp} \quad (7)$$

where the in-plane  $\epsilon_{\mathbf{k}}^{\parallel}$  and the out-of-plane  $\epsilon_{\mathbf{k}}^{\perp}$  dispersions are given by, respectively,

$$\epsilon_{\mathbf{k}}^{\parallel} = -2 \left( t \frac{\delta}{2} + \Delta \right) (\cos k_x + \cos k_y) - 4t' \frac{\delta}{2} \cos k_x \cos k_y - \mu \quad (8)$$

and

$$\epsilon_{\mathbf{k}}^{\perp} = 2t_z \frac{\delta}{2} (\cos k_x - \cos k_y)^2 \cos k_z. \quad (9)$$

The functional form  $(\cos k_x - \cos k_y)^2$  in  $\epsilon_{\mathbf{k}}^{\perp}$  is frequently invoked for cuprates [7]. Other forms for  $\epsilon_{\mathbf{k}}^{\perp}$ , however, do not change the qualitative features. Although the electronic dispersion looks similar to that in a free electron system, the hopping integrals  $t$ ,  $t'$ , and  $t_z$  are renormalised by doping  $\delta$  because of electron correlation effects. For both the optimally-doped materials we use  $\delta = 0.16$ .

The term  $\Delta$  in Eq. 8, which is proportional to  $J$ , is the mean-field value of the bond variables introduced to decouple the exchange term through a Hubbard-Stratonovich transformation [1, 6]. The value of  $\Delta$  is computed self-consistently together with the chemical potential  $\mu$  for a given  $\delta$  by using

$$\Delta = \frac{J}{4N_s N_z} \sum_{\mathbf{k}, \eta} \cos(k_{\eta}) n_F(\epsilon_{\mathbf{k}}), \quad (10)$$

and

$$(1 - \delta) = \frac{2}{N_s N_z} \sum_{\mathbf{k}} n_F(\epsilon_{\mathbf{k}}), \quad (11)$$

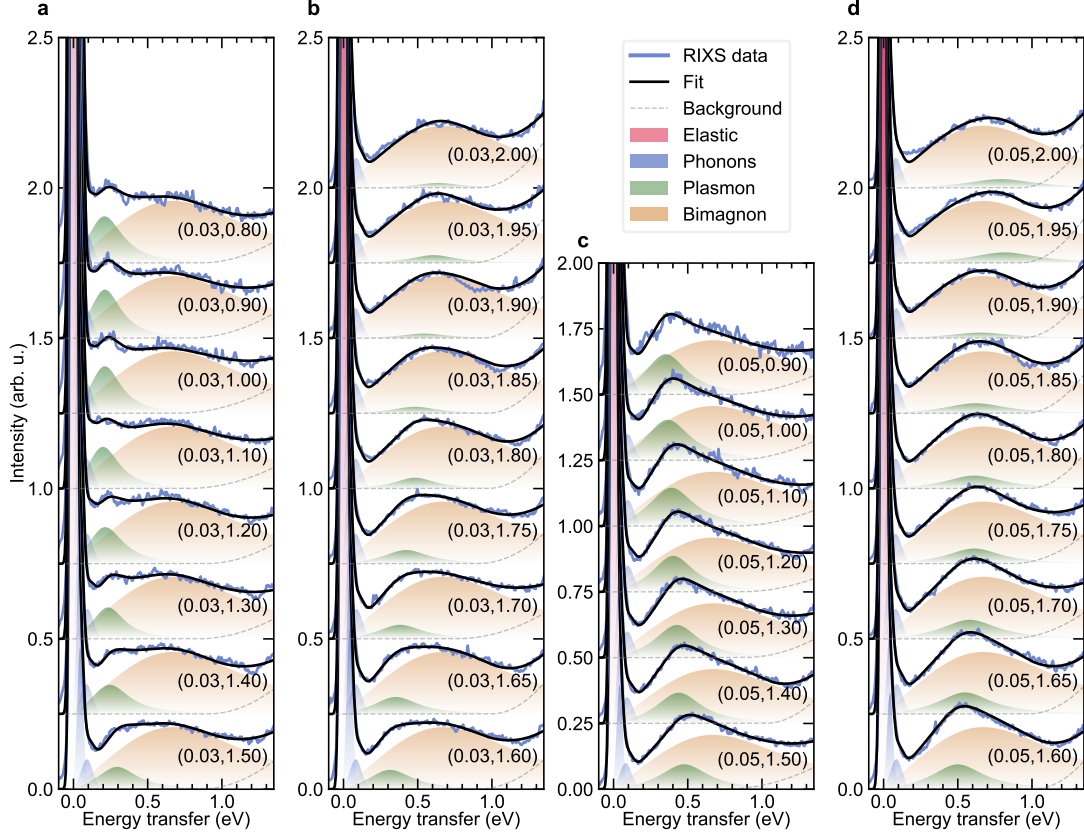


FIG. 9. **RIXS spectra fits of Bi2201 for momentum transfer along the  $l$ -direction.** **a**, **b**, **c**, and **d**, Fits to the RIXS spectra of Bi2201 presented in Fig. 3 (c, d) of main paper at mentioned  $(h, l)$ -values are shown by using the model described in Section III. The extracted plasmon peak energies have been used in Fig. 3(c, d) and Fig. 4(c) in the main paper. In Fig. 3(e) of the main paper, RIXS spectra subtracted by the fitted bimagnon contribution in this manner have been shown. The plasmon amplitudes and widths have been used in Extended Data Fig. 3 (c, f) of the main paper.

where  $n_F$  is the Fermi function, and  $N_s$  and  $N_z$  are the total number of lattice sites on the square lattice and the number of layers along the  $c$  direction respectively. We take the number of layers  $N_z$  equal to 30, which should be large enough, and set the temperature to zero.

As shown previously [1, 5, 6], the charge-charge correlation function  $\chi_c(\mathbf{r}_i - \mathbf{r}_j, \tau) = \langle T_\tau n_i(\tau) n_j(0) \rangle$  can be computed in the  $\mathbf{q}$ - $\omega$  space as

$$\chi_c(\mathbf{q}, \omega) = N \left( \frac{\delta}{2} \right)^2 D_{11}(\mathbf{q}, \omega). \quad (12)$$

Thus,  $\chi_c$  is the element (1, 1) of the  $6 \times 6$  bosonic propagator  $D_{ab}$  where

$$D_{ab}^{-1}(\mathbf{q}, i\omega_n) = [D_{ab}^{(0)}(\mathbf{q}, i\omega_n)]^{-1} - \Pi_{ab}(\mathbf{q}, i\omega_n), \quad (13)$$

and the matrix indices  $a$  and  $b$  run from 1 to 6.  $D_{ab}^{(0)}(\mathbf{q}, i\omega_n)$  is a bare bosonic propagator

$$[D_{ab}^{(0)}(\mathbf{q}, i\omega_n)]^{-1} = N \begin{pmatrix} \frac{\delta^2}{2} [V(\mathbf{q}) - J(\mathbf{q})] & \frac{\delta}{2} & 0 & 0 & 0 & 0 \\ \frac{\delta}{2} & 0 & 0 & 0 & 0 & 0 \\ 0 & 0 & \frac{4\Delta^2}{J} & 0 & 0 & 0 \\ 0 & 0 & 0 & \frac{4\Delta^2}{J} & 0 & 0 \\ 0 & 0 & 0 & 0 & \frac{4\Delta^2}{J} & 0 \\ 0 & 0 & 0 & 0 & 0 & \frac{4\Delta^2}{J} \end{pmatrix}, \quad (14)$$

and  $\Pi_{ab}$  are the bosonic self-energies,

$$\begin{aligned} \Pi_{ab}(\mathbf{q}, i\omega_n) = & -\frac{N}{N_s N_z} \sum_{\mathbf{k}} h_a(\mathbf{k}, \mathbf{q}, \varepsilon_{\mathbf{k}} - \varepsilon_{\mathbf{k}-\mathbf{q}}) \frac{n_F(\varepsilon_{\mathbf{k}-\mathbf{q}}) - n_F(\varepsilon_{\mathbf{k}})}{i\omega_n - \varepsilon_{\mathbf{k}} + \varepsilon_{\mathbf{k}-\mathbf{q}}} h_b(\mathbf{k}, \mathbf{q}, \varepsilon_{\mathbf{k}} - \varepsilon_{\mathbf{k}-\mathbf{q}}) \\ & - \delta_{a1} \delta_{b1} \frac{N}{N_s N_z} \sum_{\mathbf{k}} \frac{\varepsilon_{\mathbf{k}} - \varepsilon_{\mathbf{k}-\mathbf{q}}}{2} n_F(\varepsilon_{\mathbf{k}}), \end{aligned} \quad (15)$$

where the six-component vertex  $h_a$  is given by

$$\begin{aligned} h_a(\mathbf{k}, \mathbf{q}, \nu) = & \left\{ \frac{2\varepsilon_{\mathbf{k}-\mathbf{q}} + \nu + 2\mu}{2} + 2\Delta \left[ \cos\left(k_x - \frac{q_x}{2}\right) \cos\left(\frac{q_x}{2}\right) + \cos\left(k_y - \frac{q_y}{2}\right) \cos\left(\frac{q_y}{2}\right) \right]; 1; \right. \\ & \left. -2\Delta \cos\left(k_x - \frac{q_x}{2}\right); -2\Delta \cos\left(k_y - \frac{q_y}{2}\right); 2\Delta \sin\left(k_x - \frac{q_x}{2}\right); 2\Delta \sin\left(k_y - \frac{q_y}{2}\right) \right\}. \end{aligned}$$

Here  $\mathbf{q}$  and  $\mathbf{k}$  are three dimensional wavevectors and  $\omega_n$  is a bosonic Matsubara frequency. The factor  $N$  comes from the sum over the  $N$  fermionic channels. The 6 channels involved in  $D_{ab}(\mathbf{q}, i\omega_n)$  come from on-site charge fluctuations, fluctuations of a Lagrangian multiplier introduced to impose the non-double occupancy at any site, and fluctuations of the four bond variables which depend on  $J$  [1, 6].

To describe plasmon excitations we compute the spectral weight of the density-density correlation function  $\text{Im}\chi_c(\mathbf{q}, \omega)$  after analytical continuation

$$i\omega_n \rightarrow \omega + i\Gamma. \quad (16)$$

Since  $\Gamma$  influences the width of the plasmon, its effect on the plasmon peak position is strongest when it becomes comparable to undamped plasmon energy (overdamped condition). As observed in the experiment (see Extended Data Fig. 3(d, e) and (f)), this condition may only be true close to the zone-centre for the acoustic plasmons. Plasmon energies calculated from the optimised models, as function of  $\Gamma$ , plotted in Fig. 10(a) clearly demonstrates that plasmon dispersions have negligible effect at larger  $h$  values. Here a small positive value  $\Gamma = 0.1t$  was chosen for all the plasmon dispersion simulations. However to replicate the plasmon peak profiles observed in Fig. 3(f) of main paper,  $\Gamma$  values of  $0.2t$  and  $0.29t$  were chosen for LSCO and Bi2201 respectively. A finite value of  $\Gamma$  contains information of an extrinsic broadening due to the instrumental resolution, and an intrinsic broadening due to incoherent effects due to electronic correlations [8].

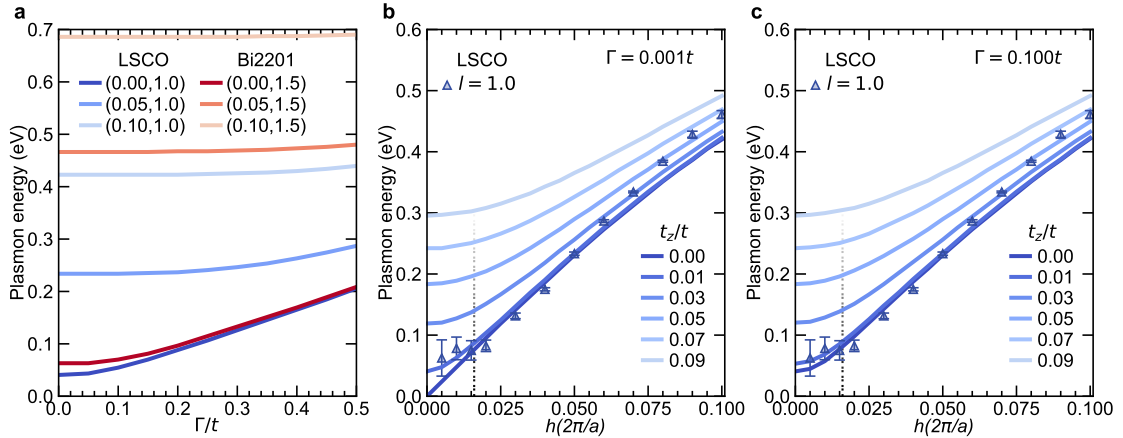


**FIG. 10. Effect of interlayer hopping on gap formation in acoustic plasmon branches** **a**, Continuous lines are plasmon energies calculated for optimised parameters for LSCO and Bi2201 at given  $(h, l)$ -values as a function of broadening parameter  $\Gamma$ . **b**, and **c**, The effect of interlayer hopping parameter  $t_z$ , on the plasmon energy gap at  $h = 0.00$ ,  $l = 1.0$  for  $\Gamma = 0.001t$  and  $\Gamma = 0.1t$  respectively. For comparison, fitted plasmon energy values from RIXS spectra collected on LSCO for  $l = 1.00$  is also shown. Two values of  $\Gamma$  are shown since it affects the plasmon energies close to the zone-center for the acoustic branches as shown in panel (a). Black dotted lines are  $h$ -values below which plasmon energies are not reliable due to large correlation with the elastic and phonon intensities.

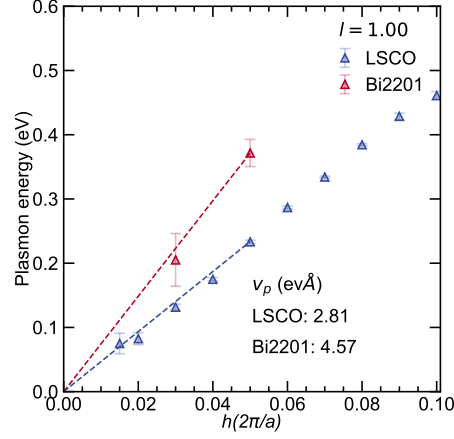


FIG. 11. **Comparison of acoustic plasmon velocities in LSCO and Bi2201** Acoustic plasmon velocities ( $v_p$ ) for LSCO and Bi2201 at  $l = 1.00$  are estimated using linear fits to extracted  $h$ -direction plasmon energies. The Bi2201 to LSCO  $v_p$  ratio is found to be around 1.6, roughly matching the ratio of the interlayer spacing between them ( $\sim 1.88$ ) [9]. The difference observed could be due to the slightly different dielectric constants of the two materials (see Methods C).

- 
- [1] Greco, A., Yamase, H. & Bejas, M. Plasmon excitations in layered high- $T_c$  cuprates. *Phys. Rev. B* **94**, 075139 (2016).
  - [2] Zhang, F. C. & Rice, T. M. Effective Hamiltonian for the superconducting Cu oxides. *Phys. Rev. B* **37**, 3759(R) (1988).
  - [3] Becca, F., Tarquini, M., Grilli, M. & Di Castro, C. Charge-density waves and superconductivity as an alternative to phase separation in the infinite-U Hubbard-Holstein model. *Phys. Rev. B* **54**, 12443 (1996).
  - [4] Thio, T. et al. Antisymmetric exchange and its influence on the magnetic structure and conductivity of  $\text{La}_2\text{CuO}_4$ . *Phys. Rev. B* **38**, 905(R) (1988).
  - [5] Greco, A., Yamase, H. & Bejas, M. Origin of high-energy charge excitations observed by resonant inelastic X-ray scattering in cuprate superconductors. *Commun. Phys.* **2**, 3 (2019).
  - [6] Foussats, A. & Greco Large- $N$  expansion based on the Hubbard operator path integral representation and its application to the  $t - J$  model. II. The case for finite  $J$ . *Phys. Rev. B* **70**, 205123 (2004).
  - [7] Andersen, O. K., Liechtenstein, A. I., Jepsen, O. & Paulsen, F. LDA energy bands, low-energy hamiltonians,  $t'$ ,  $t''$ ,  $t_\perp(k)$ , and  $J_\perp$ . *J. Phys. Chem. Solids* **56**, 1573 (1995).
  - [8] Prelovšek, P. & Horsch, P. Electron-energy loss spectra and plasmon resonance in cuprates. *Phys. Rev. B* **60**, R3735(R) (1999).
  - [9] Fetter, A. Electrodynamics of a layered electron gas. I. Single layer. *Ann. Phys.* **81**, 367 (1973).